nature physics

SUPPLEMENTARY INFORMATION

DOI: 10.1038/NPHYS3805

Imaging electrostatically confined Dirac fermions in graphene quantum dots

Juwon Lee, Dillon Wong, Jairo Velasco Jr., Joaquin F. Rodriguez-Nieva, Salman Kahn, Hsin-Zon Tsai, Takashi Taniguchi, Kenji Watanabe, Alex Zettl, Feng Wang, Leonid S. Levitov and Michael F. Crommie

TABLE OF CONTENTS:

S1. Estimating the curvature of the quadratic potential

We modelled our pn junction using the 2D massless Dirac Hamiltonian with a quadratic potential, $H = -i\hbar v_F \boldsymbol{\sigma} \cdot \nabla_{\boldsymbol{r}} - \kappa r^2$. We chose $\kappa = 6 \times 10^{-3}$ meV/nm^2, and the resulting theoretical simulation (Fig. 4b of the main text) is in good agreement with the experimental data (Fig. 4a of the main text). This value for κ was not chosen arbitrarily. We estimated κ through scanning tunnelling spectroscopy (STS) measurements of the Dirac point, with the assumption that the potential varies slowly enough that the Thomas-Fermi approximation is valid. At each point r away from the centre we performed a dI/dV_s measurement at fixed V_g such that E_D is outside of the inelastic tunnelling gap (to do this we needed to use a value of V_g that is different

DOI: 10.1038/NPHYS3805

from the value V_g = 32 V used for the data presented in Fig. 4a of the main text). We then extracted E_D through a parabolic fit, converted E_D to charge carrier density through $n(r) = E_D^2(r)/\pi(\hbar v_F)^2$, and rigidly shifted the entire $n(r)$ curve by a uniform constant to match the data at V_g = 32 V (i.e. the gate voltage in Fig. 4a of the main text). The resulting shifted $n(r)$ is plotted in Fig. S1a, and the equivalent E_D is plotted as the blue curve in Fig. S1b. A similar procedure was used to construct the n(x,y) plot in Fig. 1c of the main text (with the E_D measurement performed at V_g = 50 V, and then n(x,y) shifted to match the gate voltage held during the tip pulse). Although the data in Figs 2 and 4a of the main text are obtained from the same pn junction, the data in Fig 1c is from a different but identically prepared pn junction.

The blue curve in Fig. S1b is an approximate representation of the potential felt by Dirac quasiparticles in the pn junction of Figs 2 and 4a of the main text. We extract κ by fitting the blue curve in Fig. S1b with an even quadratic polynomial (red curve). This procedure results in $E_D(r) = (-6.33 \times 10^{-6}\ \text{eV/nm})\, r^2 + (1.05 \times 10^{-1}\ \text{eV})$, yielding $\kappa = 6 \pm 1 \times 10^{-3}\ \text{meV/nm}^2$ (corresponding to characteristic energy $\varepsilon^* = (\hbar^2 v_F^2 \kappa)^{1/3} \approx 15$ meV and characteristic length $r^* = (\hbar v_F/\kappa)^{1/3} \approx 50$ nm).

Although the potential in Fig. S1b (blue curve) deviates from the parabolic fit (red curve), this does not appear to significantly affect the agreement between the experimental and theoretical eigenstate distributions in Figs 4a and 4b of the main text. In order to understand how deviations from a parabolic potential affect our results, we simulated $\partial\text{LDOS}/\partial\varepsilon$ for a non-parabolic potential $U(r)$ whose carrier density is given by a generic shifted power law function:

$$n(r) = n_\infty - \frac{n_0}{(1 + (r/d)^2)^\gamma}.$$

Here $n_\infty = 6 \times 10^{12}\ \text{cm}^{-2}$, $n_0 = 6.9 \times 10^{12}\ \text{cm}^{-2}$, and $d = 400$ nm are phenomenological parameters determined by fitting to the experimental potential. For simplicity, we chose $\gamma = \frac{3}{2}$

(which happens to be the power law for the perfect screening of charge spatially separated from graphene[1]). In the Thomas-Fermi approximation, the potential is given by

$$U(r) = \mathrm{sgn}\big(n(r)\big)\hbar v_{\mathrm{F}}\sqrt{\pi|n(r)|}$$

The above equations for $U(r)$ and $n(r)$ fit the experimental potential quite nicely over the entire spatial range of the measurement (see green curve in Fig. S1b for fit). The resulting $\partial\mathrm{LDOS}/\partial\varepsilon$ calculated for this potential (inset in Fig. S1b) is qualitatively and quantitatively similar to $\partial\mathrm{LDOS}/\partial\varepsilon$ calculated for the parabolic potential (Fig. 4b of the main text). As such, the simple parabolic potential model is sufficient to explain our experimental results.

S2. $\mathrm{d}I/\mathrm{d}V_\mathrm{s}(V_\mathrm{g},V_\mathrm{s})$ and $\mathrm{d}I/\mathrm{d}V_\mathrm{s}(r,V_\mathrm{s})$

Figs 2d-g of the main text show $\mathrm{d}^2I/\mathrm{d}V_\mathrm{s}^2(V_\mathrm{g},V_\mathrm{s})$ measurements that were obtained by numerically differentiating $\mathrm{d}I/\mathrm{d}V_\mathrm{s}(V_\mathrm{g},V_\mathrm{s})$. Fig. S2 shows a plot of $\mathrm{d}I/\mathrm{d}V_\mathrm{s}(V_\mathrm{g},V_\mathrm{s})$ before differentiation. The red streak in the lower right corner of each plot in Fig. S2 persists inside and outside the pn junction. This spectroscopic feature may be related to graphene plasmons[2-4].

Fig. 4a of the main text shows a $\mathrm{d}^2I/\mathrm{d}V_\mathrm{s}^2(r,V_\mathrm{s})$ measurement that was obtained by numerically differentiating $\mathrm{d}I/\mathrm{d}V_\mathrm{s}(r,V_\mathrm{s})$. Fig. S3a shows a plot of $\mathrm{d}I/\mathrm{d}V_\mathrm{s}(r,V_\mathrm{s})$ before differentiation, and Fig. S3c shows $\mathrm{d}I/\mathrm{d}V_\mathrm{s}$ line cuts at fixed radial distances.

S3. $\mathrm{d}^2I/\mathrm{d}V_\mathrm{s}^2(V_\mathrm{g},V_\mathrm{s})$ and $\mathrm{d}^2I/\mathrm{d}V_\mathrm{s}^2(r,V_\mathrm{s})$ for opposite polarity pn junctions

Figs 2d-g of the main text shows $\mathrm{d}^2I/\mathrm{d}V_\mathrm{s}^2(V_\mathrm{g},V_\mathrm{s})$ for a pn junction that is p-doped at the centre and n-doped outside. Figs S4a-d show $\mathrm{d}I/\mathrm{d}V_\mathrm{s}(V_\mathrm{g},V_\mathrm{s})$ for a pn junction of the opposite heterojunction polarity (i.e. n-doped at the center and p-doped outside), and Figs S4e-h show the numerically differentiated $\mathrm{d}^2I/\mathrm{d}V_\mathrm{s}^2(V_\mathrm{g},V_\mathrm{s})$.

Fig. S5a shows $\mathrm{d}I/\mathrm{d}V_\mathrm{s}(r,V_\mathrm{s})$ for a pn junction that is n-doped at the centre and p-doped outside, and Fig. S5b shows $\mathrm{d}^2I/\mathrm{d}V_\mathrm{s}^2(r,V_\mathrm{s})$. For reasons that we do not fully understand, n-doped

DOI: 10.1038/NPHYS3805

quantum dots show poorer confinement features than the p-doped quantum dots. Nevertheless, all of our graphene quantum dots display similar oscillatory behaviour in the local density of states, with reasonably similar characteristic spatial widths and energy spacings between discrete states.

The pn junction in Fig. 3 of the main text is also n-doped at the centre and p-doped outside. Figs 3a and 3b of the main text are dI/dV_s maps of the same pn junction for different V_s and V_g, with the eigenstate in Fig. 3b having energy approximately 15 mV greater than in Fig. 3a. The pn junctions in Fig. S4, Fig. S5, and Fig. 3 of the main text are all different but are prepared in a similar manner (tip pulse at V_g = -40 V, V_s = 5 V).

S4. Procedure for creating a graphene quantum dot

1. Set V_s = -0.5 V and I = 0.5 nA. Close the scanning tunnelling microscope (STM) feedback loop.
2. To create a graphene quantum dot that is p-doped (n-doped) at the centre, set V_g = 40 V (-40 V). Using other values of V_g will lead to different values of doping.
3. Open the STM feedback loop.
4. Withdraw the STM tip by $\Delta z \sim 1.5$ - 2 nm.
5. Increase V_s to +5 V.
6. Wait 1 minute.
7. Decrease V_s to -0.5 V.
8. Close the STM feedback loop.

S5. Tip height dependence in dI/dV_s maps

A dI/dV_s map (at a fixed V_s) measures the local density of states (LDOS) as a function of (x,y):

$$\frac{dI}{dV_s}(x,y) = A(z) * \mathrm{LDOS}(x,y,z_0,E_F+eV_s)$$

where $A(z)$ is a proportionality factor that depends on the tip-sample distance (and z_0 is a fixed tip-sample distance). Since the dI/dV_s map in Fig. 2c of the main text was obtained using constant-current feedback, the tip height z will change as a function of (x,y) to ensure

$$I_0 = \left|\int_0^{V_s} \frac{dI}{dV} dV\right| = A(z)\left|\int_0^{V_s} \mathrm{LDOS}(x,y,z_0,E_F+eV)dV\right|$$

where $I_0 = 0.5$ nA is the tunnelling current setpoint. Therefore

$$A(z) = \frac{I_0}{\left|\int_0^{V_s} \mathrm{LDOS}(x,y,z_0,E_F+eV)dV\right|}$$

and thus

$$\frac{dI}{dV_s}(x,y) = I_0 \frac{\mathrm{LDOS}(x,y,z_0,E_F+eV_s)}{\left|\int_0^{V_s} \mathrm{LDOS}(x,y,z_0,E_F+eV)dV\right|}$$

It is clear that dI/dV_s is related to LDOS but is not directly proportional to LDOS (see Wittneven *et al.*[5] for more details). This explains the contrast between the p-doped and n-doped regions in Fig. 2c of the main text. Figure S6 shows two dI/dV_s curves at $r = 0$ nm (blue curve) and $r = 200$ nm (red curve). Both curves have a ~130 meV gap-like feature at the Fermi energy caused by phonon-assisted inelastic tunnelling[6] and a local minimum (labelled by coloured arrows) that indicate the Dirac point. Note that dI/dV_s is adjusted such that the area under both curves from V_s = -0.25 V to $V_s = 0$ V is equal to $I_0 = 0.5$ nA (this is the constant-current feedback condition), resulting in higher dI/dV_s at V_s = -0.25 V (the tunnelling bias setpoint for Fig. 2c of the main text) for the n-doped curve compared to the p-doped curve.

S6. Resonance widths

DOI: 10.1038/NPHYS3805

A confined state in an electrostatic graphene quantum dot is quasi-bound in the sense that it has a finite lifetime τ due to coupling to the continuum via Klein tunnelling. This "leakage" of the quantum dot can be quantified via the widths of the resonance peaks $\hbar/\tau$. To accurately obtain the intrinsic widths, we chose a simulation size L and Lorentizan broadening $\Gamma \sim \hbar v_F/L$ such that $\Gamma < \hbar/\tau$ (see Methods). Except for the (0, ½) state (which has a width ~15 meV in theory and experiment), the linewidths in both the experimental data and the simulation lie in the range 4 meV ≤ width ≤ 10 meV (corresponding to lifetimes 2 x 10^{-13} s ≥ τ ≥ 7 x 10^{-14} s), with resonances that exhibit higher angular momenta displaying lower widths (longer lifetimes) than states with lower angular momenta. This is consistent with the idea that (due to Klein tunnelling) higher angular momentum states are more easily trapped by circular electrostatic potentials in graphene[7,8].

Although our experimental and theoretical resonance widths are in good agreement, future studies may be required to fully disentangle the lifetimes due to Klein tunnelling and many-body effects. For example, angle-resolved photoemission spectroscopy (ARPES)[9] and theoretical calculations[10] have shown that the contribution to the imaginary part of the electron self-energy from electron-electron interactions can be significant in the energy range of our scanning tunnelling spectroscopy experiments.

1. Fogler, M.M., Novikov, D.S. & Shklovskii, B.I. Screening of a hypercritical charge in graphene. *Phys. Rev. B* **76**, 233402 (2007).
2. Bostwick, A. *et al.* Observation of Plasmarons in Quasi-Freestanding Doped Graphene. *Science* **328**, 999-1002 (2010).
3. Principi, A., Polini, M., Asgari, R. & MacDonald, A.H. The tunneling density-of-states of interacting massless Dirac fermions. *Solid State Commun.* **152**, 1456-1459 (2012).
4. Lischner, J., Vigil-Fowler, D. & Louie, S.G. Physical Origin of Satellites in Photoemission of Doped Graphene: An *Ab Initio* GW Plus Cumulant Study. *Phys. Rev. Lett.* **110**, 146801 (2013).

5. Wittneven, C., Dombrowski, R., Morgenstern, M. & Wiesendanger, R. Scattering States of Ionized Dopants Probed by Low Temperature Scanning Tunneling Spectroscopy. *Phys. Rev. Lett.* **81**, 5616-5619 (1998).
6. Zhang, Y. *et al.* Giant phonon-induced conductance in scanning tunnelling spectroscopy of gate-tunable graphene. *Nature Phys.* **4**, 627-630 (2008).
7. Wu, J.-S. & Fogler, M.M. Scattering of two-dimensional massless Dirac electrons by a circular potential barrier. *Phys. Rev. B* **90**, 235402 (2014).
8. Zhao, Y. *et al.* Creating and probing electron whispering-gallery modes in graphene. *Science* **348**, 672-675 (2015).
9. Siegel, D.A. *et al.* Many-body interactions in quasi-freestanding graphene. *Proc. Natl Acad. Sci. USA* **108**, 11365-11369 (2011).
10. Brar, V.W. *et al.* Observation of Carrier-Density-Dependent Many-Body Effects in Graphene via Tunneling Spectroscopy. *Phys. Rev. Lett.* **104**, 036805 (2010).

DOI: 10.1038/NPHYS3805

FIGURE S1

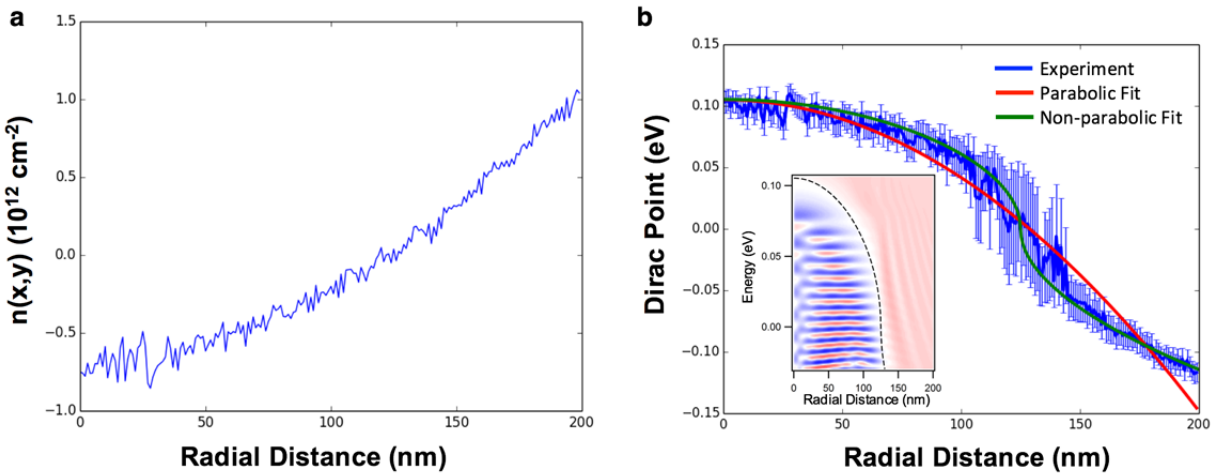

Figure S1 | Circular electrostatic potential. a, Charge carrier density for the pn junction in Fig. 2 and Fig. 4a of the main text. **b**, Dirac point energy (blue curve) corresponding to **a**. The Dirac point energy is fit with a quadratic polynomial with curvature $\kappa = 0.006$ meV/nm^2 (red curve). This value of κ is used to generate the theoretical simulation in Fig. 4b of the main text. The green curve is a shifted power law fit to the experimental blue curve. The inset is $\partial \mathrm{LDOS}/\partial \varepsilon$ calculated for the non-parabolic potential represented by the green curve (which is also the dashed line in the inset).

FIGURE S2

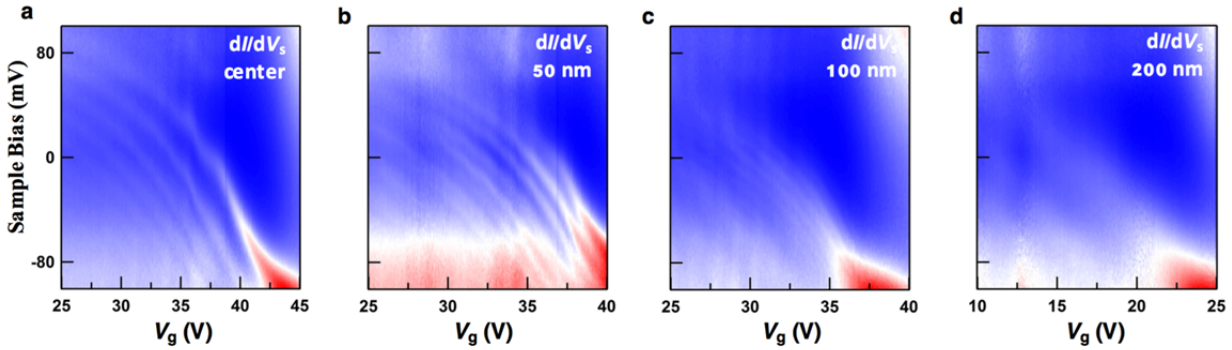

Figure S2 | dI/dV_s(V_g,V_s) plots used to calculate d^2I/dV_s^2(V_g,V_s) shown in Figs 2d-g of the main text.

DOI: 10.1038/NPHYS3805

FIGURE S3

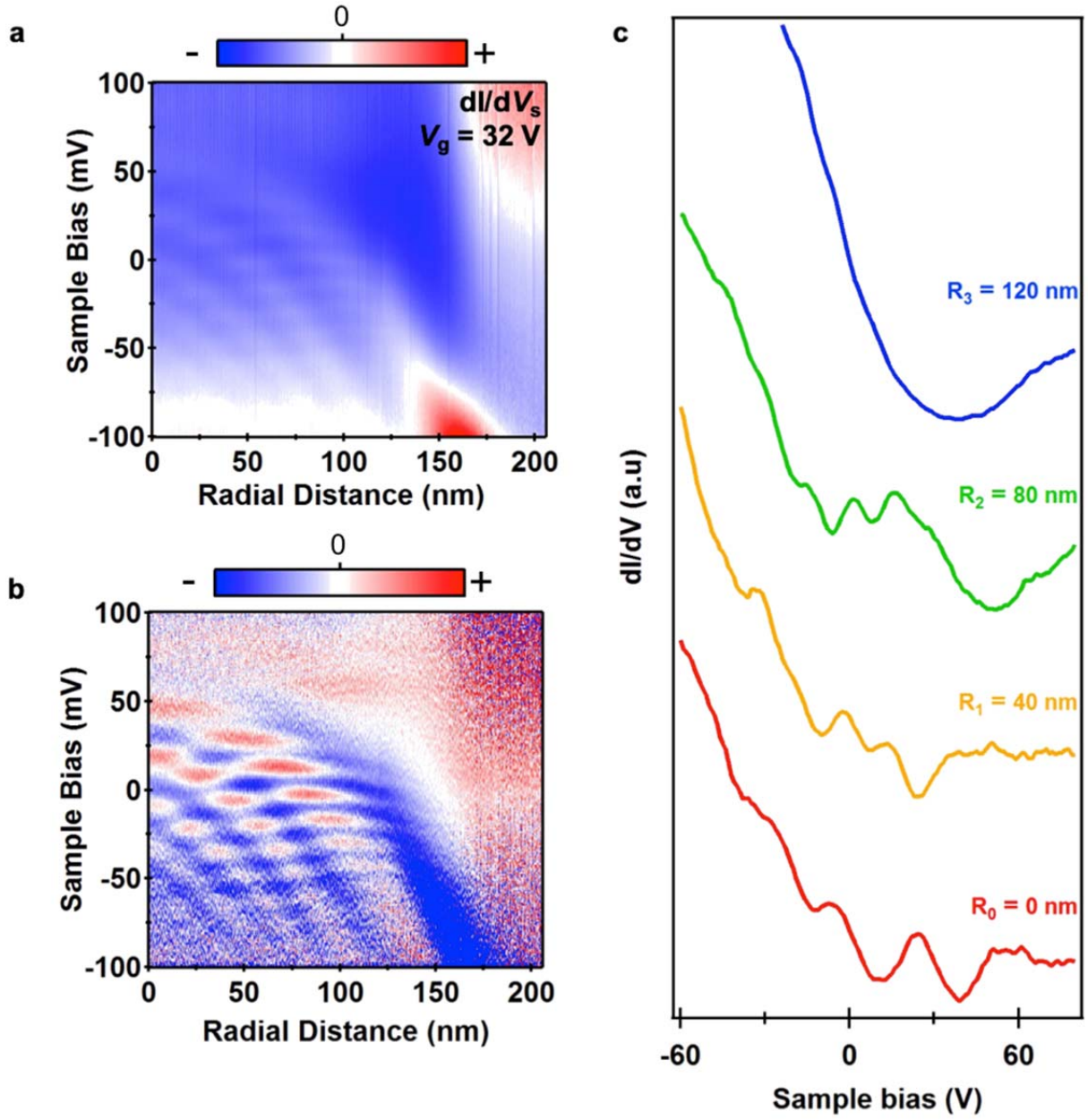

Figure S3 | dI/dV_s(r,V_s) plot used to calculate d^2I/dV_s^2(r,V_s) shown in Fig. 4a of the main text. a, dI/dV_s(r,V_s) plot showing faint horizontal features modulated by a parabolic envelope. **b**, d^2I/dV_s^2(r,V_s) obtained by numerically differentiating **a**. **c**, dI/dV_s line cuts at fixed radial distances showing discrete states at fixed energies.

FIGURE S4

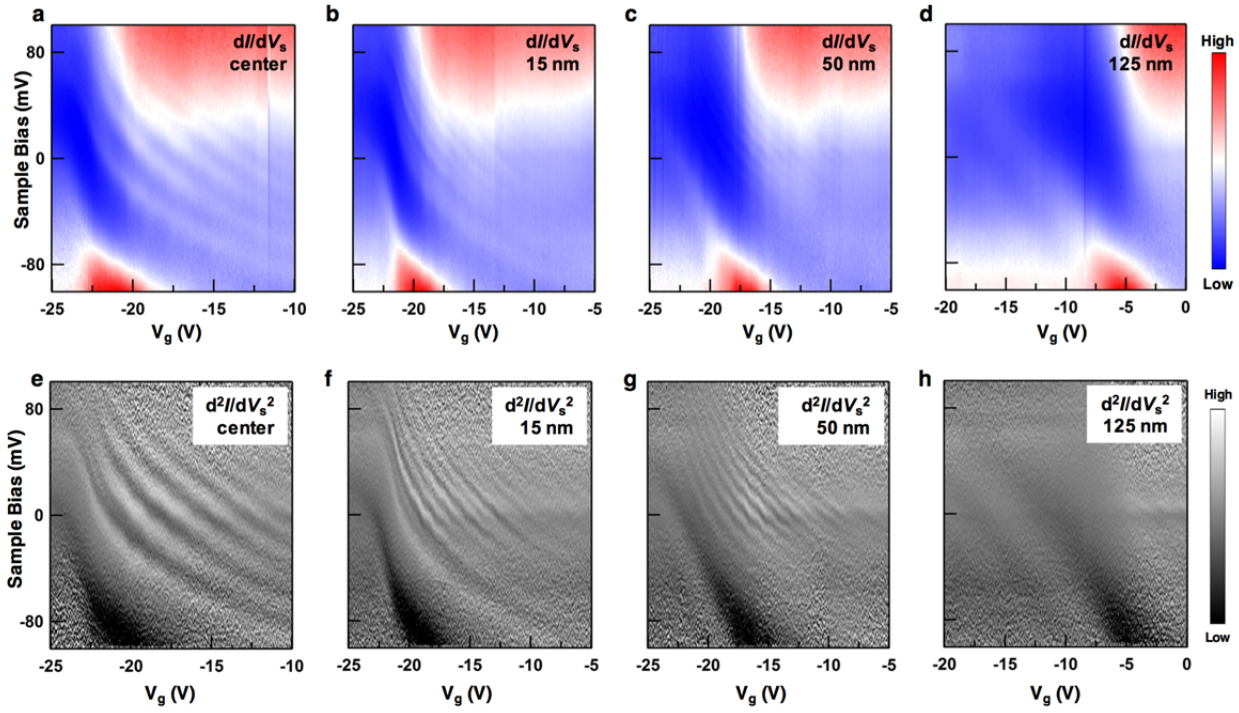

Figure S4 | Gate-tuneable STS measurements of pn junction with opposite polarity. a-d, $dI/dV_s(V_g,V_s)$ for a pn junction that is n-doped at the centre and p-doped outside. **e-f**, $d^2I/dV_s^2(V_g,V_s)$ obtained by numerically differentiating **a-d**.

DOI: 10.1038/NPHYS3805

FIGURE S5

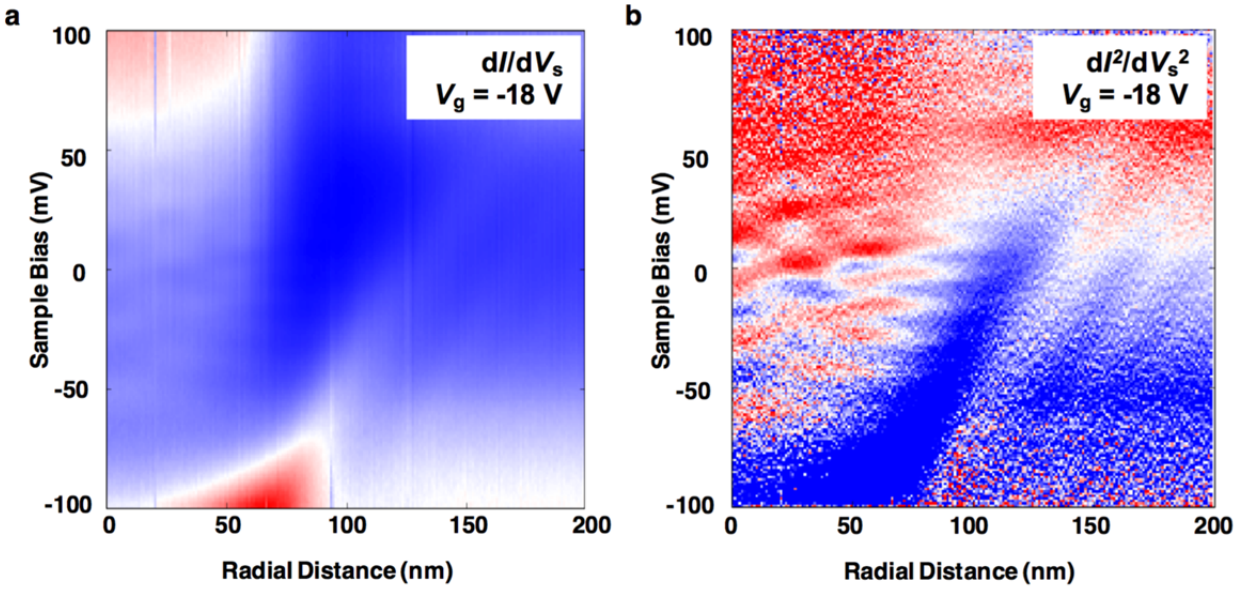

Figure S5 | Spatially resolved energy level spectrum of pn junction with opposite polarity. **a**, $dI/dV_s(r,V_s)$ for a pn junction that is n-doped at the centre and p-doped outside. **b**, $d^2I/dV_s^2(r,V_s)$ obtained by numerically differentiating **a**.

FIGURE S6

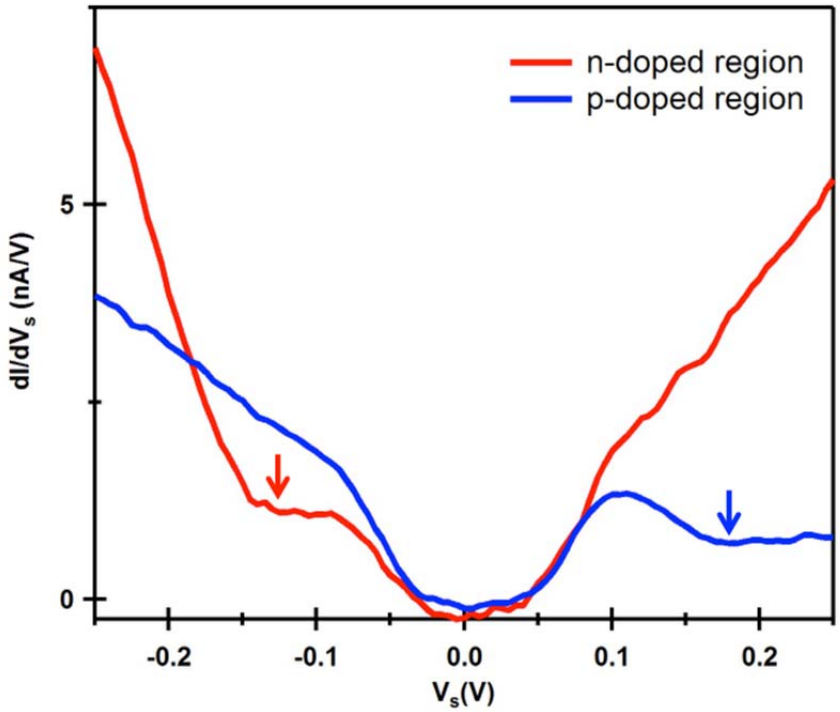

Figure S6 | dI/dV_s curves showing a pn junction. The blue curve is obtained at the centre (r = 0 nm) of the pn junction in Fig. 2c of the main text. The red curve is obtained at r = 200 nm away from the centre. The coloured arrows represent the local graphene Dirac point. Note the scaling such that the V_s-integrated area under both curves from V_s = -0.25 V to V_s = 0 V is equal to I_0 = 0.5 nA, reflecting the constant-current feedback condition employed in standard STM operation. This results in higher dI/dV_s at V_s = -0.25 V (the tunnelling bias setpoint for Fig. 2c of the main text) for the red curve (r = 200 nm) compared the blue curve (r = 0 nm).